Small

NANO · MICRO small
www.small-journal.com

RESEARCH ARTICLE

ZIF-8 Film Coatings Render Polymeric Device Surfaces Addressable by $^{1}H/^{129}Xe$ MRI

Xinxin Yang[1,2] | Qingbin Zeng[1,2] | Jiawei Zhu[1,3] | Xiuchao Zhao[1,2] | Zhen Wang[1,2] | Zhongyu Xiao[1,2] | Yanling Feng[1,3] | Yaping Yuan[1,2] | Chenlu Yuan[1,2] | Haidong Li[1,2] | Sa Xiao[1,2] | Louis-S. Bouchard[4] | Xin Zhou[1,2,5] | Qianni Guo[1,2]

[1]State Key Laboratory of Magnetic Resonance Spectroscopy and Imaging, National Center for Magnetic Resonance in Wuhan, Wuhan Institute of Physics and Mathematics, Innovation Academy for Precision Measurement Science and Technology, Chinese Academy of Sciences, Wuhan, People's Republic of China | [2]University of Chinese Academy of Sciences, Beijing, People's Republic of China | [3]College of Life Science and Technology, Huazhong University of Science and Technology, Wuhan, People's Republic of China | [4]Department of Chemistry and Biochemistry, The Molecular Biology Institute, Jonsson Comprehensive Cancer Center, California NanoSystems Institute, University of California, Los Angeles, USA | [5]School of Biomedical Engineering, Hainan University, Haikou, People's Republic of China

Correspondence: Xin Zhou (xinzhou@wipm.ac.cn) | Qianni Guo (qian-niguo@wipm.ac.cn)

Received: 28 July 2026 | **Revised:** 1 September 2026 | **Accepted:** 4 September 2026

Keywords: hyperpolarized xenon MRI | metal-organic framework film | polymeric device coatings | xenon-addressable surface labeling | ZIF-8 film

ABSTRACT

Metal-organic framework (MOF) films synergize molecular-scale porosity with conformal surface chemistry on polymer substrates. We report a spectrally selective coating in which a ZIF-8 film, seeded by a Zn(II)-polydopamine (Zn-PDA) interlayer on polytetrafluoroethylene (PTFE), enables hyperpolarized ^{129}Xe MRI detection of the polymer surface, while conventional ^{1}H MRI delineates anatomy. The coating produces a film-bound ^{129}Xe resonance at 82.0 ppm in both water and fetal bovine serum. After 60 min, the resonance position remained unchanged, with signal-to-noise ratios decreasing by only 14.9% and 17.2%, respectively. Selective excitation yields coating-specific positive contrast on the ^{129}Xe channel; correspondingly, ^{1}H MRI reveals a distinct surface appearance likely due to altered local proton density and magnetic susceptibility. In phantoms, ^{129}Xe and ^{1}H images were co-registered with a center-point offset of 0.34 mm; in a flow simulator, the offset was 0.26 mm. A rat airway experiment confirmed in vivo spectral selectivity with a film-bound resonance near 92 ppm, co-localizing with ^{129}Xe ventilation and ^{1}H anatomical references. While demonstrated here using coated PTFE segments and direct xenon bubbling, these results provide a robust proof of concept for MOF-coated polymers as spectrally selective ^{129}Xe MRI labels, warranting future physiological translation.

1 | Introduction

Metal–organic frameworks (MOFs) are crystalline porous coordination solids built from metal nodes and organic linkers. Their high internal surface area, tunable pore apertures, and modular composition support applications in gas storage and separation, catalysis, and sensing [1–4]. MOF thin films have also been prepared for device functions such as photodetection [5], and MOF particles have been investigated as magnetic resonance imaging (MRI) contrast agents and therapeutic materials [6–8]. In MRI, paramagnetic metal ions such as Gd^{3+}, Mn^{2+}, and Fe^{3+} can modulate longitudinal or transverse relaxation [6, 7]. By contrast, MOF films remain less explored as functional coatings on biomedical polymer surfaces. Such coatings must be conformal

Xinxin Yang and Qingbin Zeng contributed equally to this work.

and adherent, and they must retain the accessible porosity needed for signal generation over the imaging window.

MRI-guided device visualization requires conspicuity without unacceptable radiofrequency (RF) heating or image distortion. MRI-visible guidewires are commonly divided into active and passive designs. Active devices often use nickel–titanium cores and a polymer cover, with conductors or small RF coils integrated into the device [9–13]. These components can provide a strong signal but also create pathways for RF coupling and heating [14, 15]. Passive devices avoid electrical conductors and instead use susceptibility markers such as Bayoxide E8706 [16], iron particles [17, 18], superparamagnetic iron oxide nanoparticles [19, 20], iron oxide [21], iron-platinum alloy nanoparticles [22], or dysprosium oxide [23] on the polymer cover. These devices can reduce RF coupling, but susceptibility contrast can be weak or can broaden the apparent device profile and obscure nearby anatomy. A surface coating that can be interrogated on a spectrally separated channel could therefore provide positive coating-specific contrast while preserving the ^{1}H image for anatomy.

Hyperpolarized (HP) ^{129}Xe MRI increases sensitivity by creating non-Boltzmann spin polarization through spin-exchange optical pumping [24, 25]. HP ^{129}Xe is widely used for lung imaging, including measurements of ventilation [26–30], microstructure [31, 32], and gas exchange [33–36]. Dissolved ^{129}Xe can also be detected in perfused compartments such as blood, heart, and brain. These features suggest that a xenon-addressable surface could be localized selectively with ^{129}Xe MRI while ^{1}H MRI supplies anatomical context. Previous work from our group showed that selected MOFs, including ZIF-8, capture HP ^{129}Xe in aqueous media and produce shifted entrapped-xenon NMR signals [37–39]. The scientific question is whether a surface-anchored film can preserve a spectrally resolved xenon response after heterogeneous growth on an inert polymer. ZIF-8 was selected here because it combines hydrophobic micropores, a resolvable ^{129}Xe resonance, high host density, and established heterogeneous growth chemistry on Zn(II)-polydopamine (Zn-PDA) layers [37–42]. Compared with other xenon hosts, including cryptophanes [43], nanoemulsions [44], gas vesicles [45], cucurbit[6]uril [46], Fe_4L_6 cages [47], and beta-lactamase reporters [48], ZIF-8 serves as an attractive starting point for this concept because it can be grown directly as a dense, adherent film on Zn-PDA-modified polytetrafluoroethylene (PTFE) under mild conditions; it retains a resolved ^{129}Xe resonance even in the solid state and aqueous environments; and its film growth is synthetically straightforward. These features make ZIF-8 a practical model host to test the concept of surface-selective ^{129}Xe MRI labeling of polymeric device surfaces, and they provide a foundation for extending this strategy to other xenon-host coatings in future studies.

Here we describe a materials-and-imaging proof of concept for a MOF-film surface label on polymeric device covers. Zn(II)-doped polydopamine was used to seed ZIF-8 growth on PTFE, yielding a coated segment denoted ZIF-8@PTFE (Figure 1). The ZIF-8 film captures HP ^{129}Xe and alters the local ^{1}H appearance of the coated surface. In vitro, selective excitation of the film-bound ^{129}Xe signal (^{129}Xe@ZIF-8) produced coating-selective ^{129}Xe images that co-registered with ^{1}H anatomy with a center-point offset of 0.34 mm. A flow simulator and a rat airway experiment tested localization during bulk flow and in a living gas-contact environment, respectively. We intentionally frame the study as a coated-surface imaging demonstration, not as validation of a complete interventional guidewire. Translation to vascular use will require physiological xenon delivery, complete-device construction, mechanical durability testing under abrasion and vascular shear, particle-detachment analysis, and extended blood-contact studies.

2 | Results and Discussion

2.1 | Fabrication Strategy and Characterization of ZIF-8@PTFE

The goal of this study was to assess the ^{1}H/^{129}Xe MRI contrast generated by a ZIF-8 film on a guidewire-cover surrogate, rather than to fabricate a complete guidewire. The cover of many MRI-compatible guidewires is PTFE shrink tubing because of its lubricity and blood compatibility [17, 18, 40]. We therefore used PTFE shrink tubes cut into approximately 8 cm segments and developed a surface-growth route for ZIF-8. A Zn-PDA interlayer promoted surface nucleation. After coating with Zn-PDA, the surface was activated with 2-methylimidazole (2-MI) in water to form ZIF-8 seeds, followed by solvothermal growth of an intergrown ZIF-8 film [41, 42] (Figure 2a).

Scanning electron microscopy (SEM) documented each step (Figure 2b–e). Pristine PTFE exhibited microcracks (Figure 2b). The Zn-PDA treatment covered these defects and produced a granular layer with ~25 nm features (Figure 2c). Energy-dispersive X-ray spectroscopy (EDX) detected Zn on the coated surface (Figure S1), and attenuated total reflectance Fourier-transform infrared spectroscopy (ATR-FTIR) showed a weak band at 1490 cm^{-1} and a broad 3100–3500 cm^{-1} envelope consistent with –OH/–NH_2 stretches of Zn-PDA (Figure S2) [41, 49, 50]. Since the ultrathin Zn-PDA interlayer on PTFE is inaccessible to direct X-ray photoelectron spectroscopy (XPS), powder references of PDA and Zn-PDA were employed, in which the Zn(II)-O coordination with catechol/benzoquinone groups confirmed the anchoring of Zn^{2+} nucleation sites for subsequent ZIF-8 growth. (Figure S3). After 2-MI activation, hexagonal ZIF-8 seeds (~40–70 nm) were visible on the Zn-PDA layer (Figure 2d). Subsequent solvothermal growth yielded intergrown ZIF-8 crystallites that formed a compact film on PTFE (Figure 2e). Small intergranular gaps were present. Cross-sectional SEM showed a film thickness of ~8 μm (Figure S4).

Powder X-ray diffraction (PXRD) of ZIF-8@PTFE segments showed reflections attributable to both ZIF-8 and the PTFE substrate, consistent with ZIF-8 phase formation on the surface (Figure 2f) [51, 52]. Nitrogen sorption isotherms were type I for both the ZIF-8 film sample and the reference ZIF-8 powder, with similar micropore size distributions (Figure 2g and inset) [51, 52]. The Brunauer–Emmett–Teller (BET) surface area and micropore volume reported for the film sample were 1709 m^2 g^{-1} and 0.64 cm^3 g^{-1}, respectively, close to those of ZIF-8 powder (1885 m^2 g^{-1} and 0.73 cm^3 g^{-1}); these values should be interpreted as normalized to the ZIF-8-containing fraction rather than to the full PTFE composite mass. ATR-FTIR detected ZIF-8 vibrational bands at 420 cm^{-1} (Zn-N stretching), 994 cm^{-1}, and 1146 cm^{-1} on ZIF-8@PTFE (Figure S2). Photographs showed macroscopically

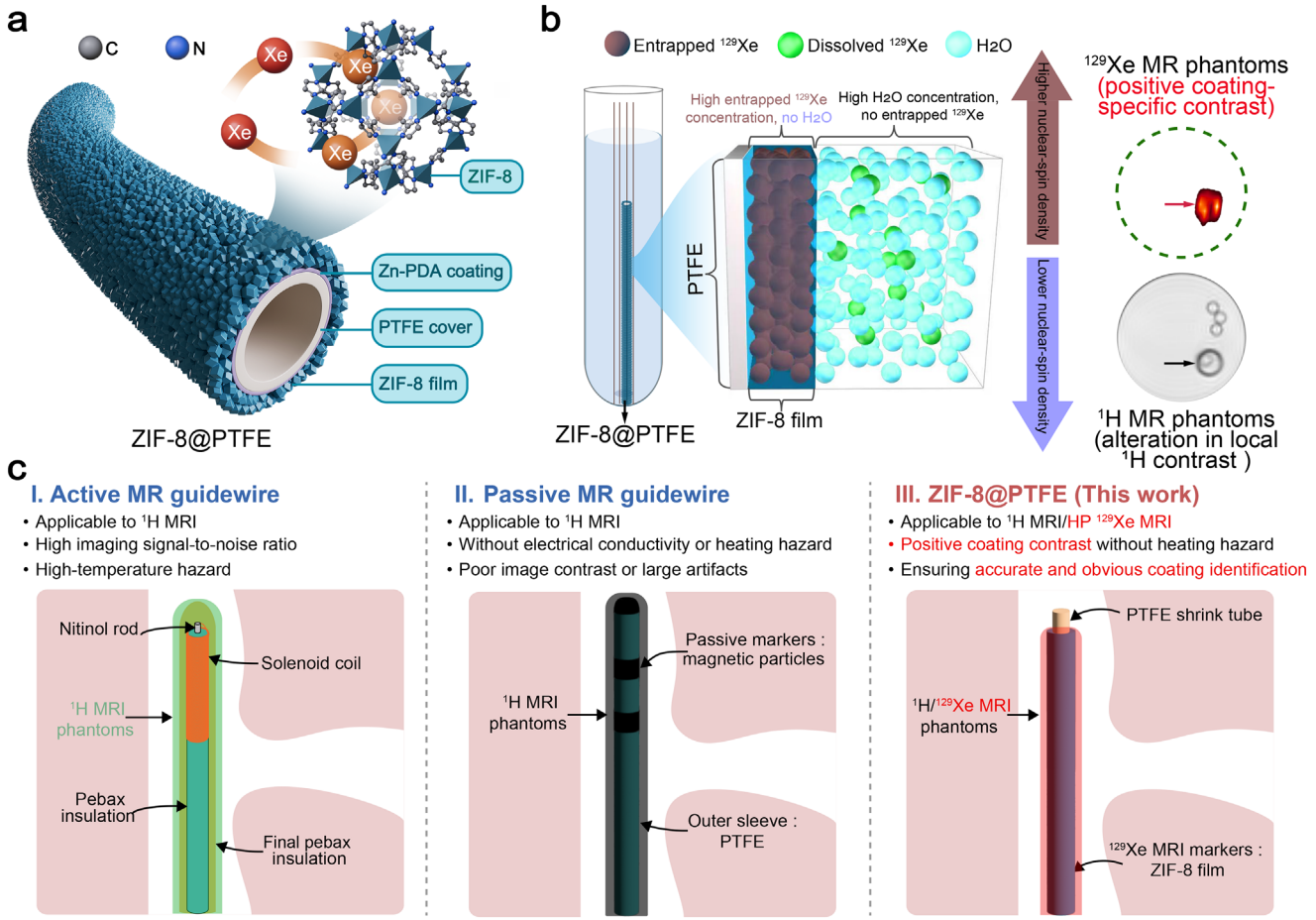

FIGURE 1 | Schematic illustration of ZIF-8@PTFE surface labeling and comparison with common MR guidewire visibility modes. (a) Structural diagram of ZIF-8@PTFE. (b) ZIF-8@PTFE in aqueous solution and the corresponding ^{129}Xe/^{1}H MRI concept. The ZIF-8 film captures ^{129}Xe and produces a spectrally shifted entrapped-xenon signal, while the porous coating alters local ^{1}H contrast. (c) Schematic comparison of active MR guidewire, passive MR guidewire, and ZIF-8@PTFE surface-labeling concepts.

continuous film coverage (Figure 2h). SEM images after 0.5 h immersion in water, plasma, or serum showed no obvious loss of surface morphology (Figures S5 and S6). However, morphology alone does not establish retention of crystallinity, Zn-N coordination, or accessible microporosity. To address these questions, we performed a series of additional experiments after 60 min of immersion in water or fetal bovine serum (FBS). First, the Zn 2p, N 1s, and O 1s binding energies changed negligibly after immersion, and no additional resolved components were observed. These ex situ XPS data are consistent with retention of the predominant surface chemical environment but do not exclude partial delamination or minor zinc species (Figure S7). ATR-FTIR bands at 421, 994, and 1146 $cm^{-1,}$ and the PXRD pattern showed no major changes after immersion, consistent with retention of the predominant ZIF-8 structure over 60 min (Figures S8 and S9). Nitrogen adsorption-desorption tests revealed only mild reductions in BET surface area and micropore volume (Figures S10 and S11). ICP-OES detected Zn^{2+} concentrations of 5.79 and 12.55 μg mL^{-1} after 0.5 and 1 h, respectively, corresponding to estimated ZIF-8 mass losses of 2.89% and 6.23% (Table S1). Second, hemolysis ratios were low under the tested short-term conditions (Figure S12) [53, 54], and the blood clotting index (BCI) of ZIF-8@PTFE was slightly higher than that of the PBS control group (a higher BCI indicates less clot formation), indicating no increase in clot formation relative to PBS under this static, short-term assay (Figure S13). Third, a bending durability test was performed to evaluate the mechanical integrity of the ZIF-8 film. After 100 cycles of bending at a 45° angle, optical microscopy revealed no visible cracks, delamination, or detachment of the ZIF-8 film from the PTFE substrate (Figure S14). These observations provide preliminary evidence that the coating tolerates moderate bending under the tested conditions. Together, these data show that the retained film remains predominantly crystalline and microporous over the 60 min test window, while the measured zinc release and the limited mechanical and blood-contact assays preclude conclusions about long-term stability or device safety.

2.2 | In Vitro Localization of ZIF-8@PTFE

Before localization experiments, we tested whether ZIF-8@PTFE segments (thick segment: outer diameter, 1.34 mm; inner diameter, 1.0 mm) produced a film-bound ^{129}Xe signal suitable for selective imaging. Segments were placed at the bottom of a 10 mm NMR tube, and HP ^{129}Xe was bubbled through four fused-silica capillaries before acquisition. ZIF-8@PTFE produced film-bound resonances (^{129}Xe@ZIF-8) when exposed to HP ^{129}Xe in gas, water,

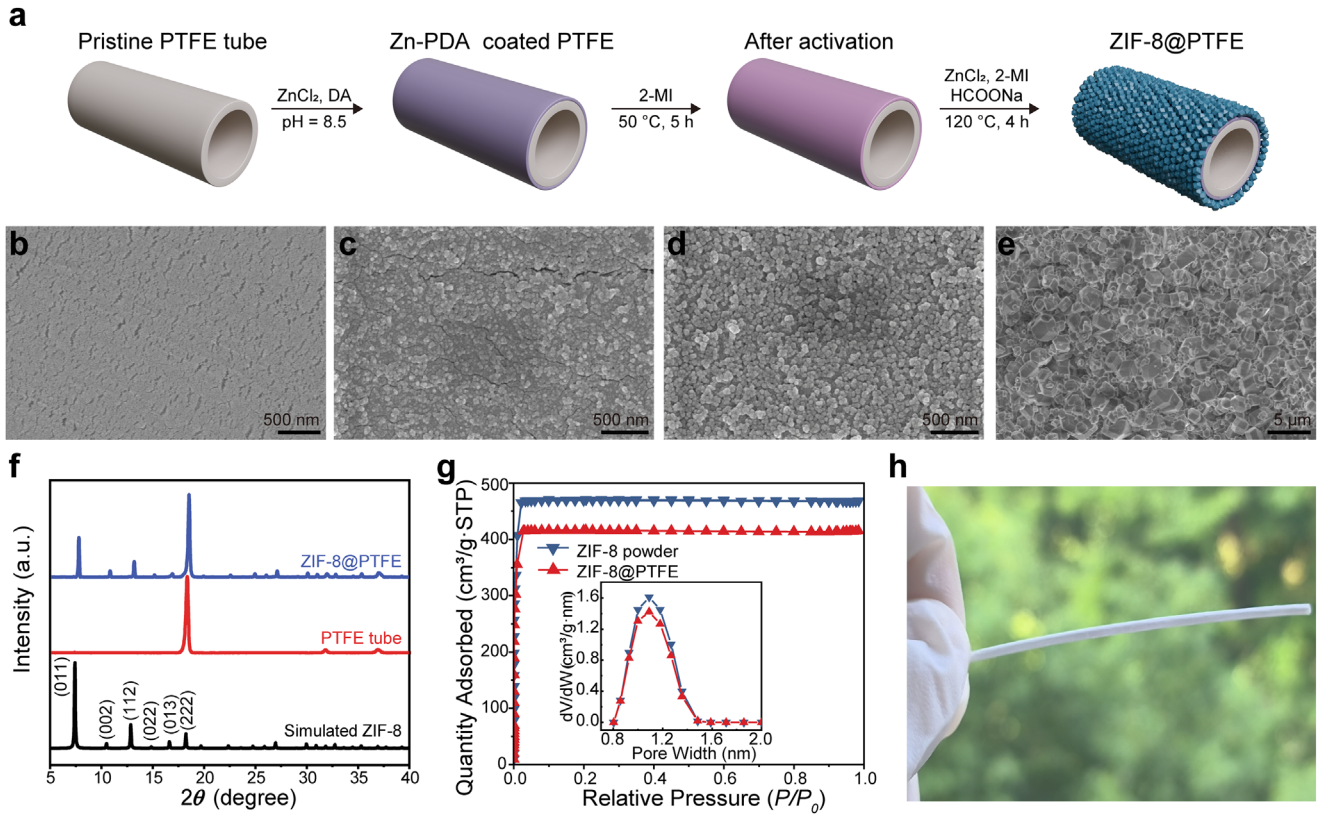

FIGURE 2 | Stepwise fabrication and characterization of ZIF-8@PTFE. (a) Schematic of the preparation process. Top-view SEM images of (b) pristine PTFE, (c) Zn-PDA-coated PTFE, (d) 2-MI-activated Zn-PDA-coated PTFE, and (e) ZIF-8@PTFE. (f) PXRD patterns of pristine PTFE and ZIF-8@PTFE. (g) Nitrogen adsorption-desorption isotherms of the ZIF-8 film sample and ZIF-8 powder; inset, corresponding micropore-size distributions. (h) Photograph of ZIF-8@PTFE.

and FBS (Figure 3a). The film-bound peak appeared at 82.0 ppm in water and FBS and at ~83 ppm in gas, with the highest intensity under gas exposure. At matched nominal ZIF-8 mass and acquisition settings, the film-bound ^{129}Xe signal from ZIF-8@PTFE was modestly lower than that from the powder reference, consistent with retained pore accessibility in the approximately 8 μm film. The full widths at half maximum (FWHM) for ZIF-8@PTFE (128 Hz, entrapped; 48 Hz, dissolved) were narrower than those for pristine ZIF-8 (212 Hz, entrapped; 492 Hz, dissolved) (Figure S15). Linewidth differences can arise from exchange, relaxation, susceptibility, and sample geometry; the present measurements do not isolate these contributions. The apparent T_1 relaxation time of film-bound ^{129}Xe was 136 s in water for the thick ZIF-8@PTFE sample (Figure S16). The trapping behavior was comparable to that reported previously for ZIF-8 nanoparticles [38, 39]. The entrapped ^{129}Xe signal-to-noise ratio (SNR) varied across ten consecutive acquisitions in water but exhibited no systematic decay (Figure 3b and Figure S17). After 60 min of incubation in water or FBS, the SNR decreased by 14.9% and 17.2%, respectively, while the ^{129}Xe chemical shift remained constant at 82 ppm (Figures S18 and S19). These results indicate that the film can be repeatedly interrogated with hyperpolarized ^{129}Xe over the measurement window, with no evidence of progressive signal loss or spectral drift. We then evaluated ^{1}H/^{129}Xe MRI in water. Selective excitation at the film-bound ^{129}Xe frequency (^{129}Xe@ZIF-8, ~82.0 ppm) produced coating-specific ^{129}Xe images (Figure 3c). In parallel, the coated surface showed a 30.71% higher ^{1}H contrast-to-noise ratio (CNR) than pristine PTFE under the stated acquisition and analysis conditions (Figure S20). The origin of this contrast was not isolated and may include changes in local proton density and susceptibility near the coating. The ^{129}Xe images were co-registered with the ^{1}H images with a center-point offset of 0.34 mm in the axial plane (Figure 3c). Pristine PTFE without ZIF-8 produced no detectable film-bound ^{129}Xe signal (Figure S21), showing that pristine PTFE does not generate the observed coating-selective ^{129}Xe response.

2.3 | Localization of ZIF-8@PTFE in a Flow Simulator

To test film-bound ^{129}Xe detection under flow, we built a benchtop flow simulator (Figure 4a). ZIF-8@PTFE segments were fixed inside a 10 mm glass tube and perfused with a model fluid adjusted to a viscosity of 3 mPa s using a peristaltic pump. During acquisition, HP ^{129}Xe was bubbled directly into the tube through four fused-silica capillaries. This configuration is not physiological, because vascular xenon delivery would occur through dissolved xenon transported by blood after pulmonary gas exchange. The simulator instead provides a controlled test of film-bound ^{129}Xe detection during bulk flow; it does not reproduce physiological xenon delivery, blood composition, or vascular shear.

The ZIF-8 film produced a film-bound ^{129}Xe peak at 82.4 ppm both without flow (SNR 14.31) and with flow (SNR 3.86) (Figure 4b).

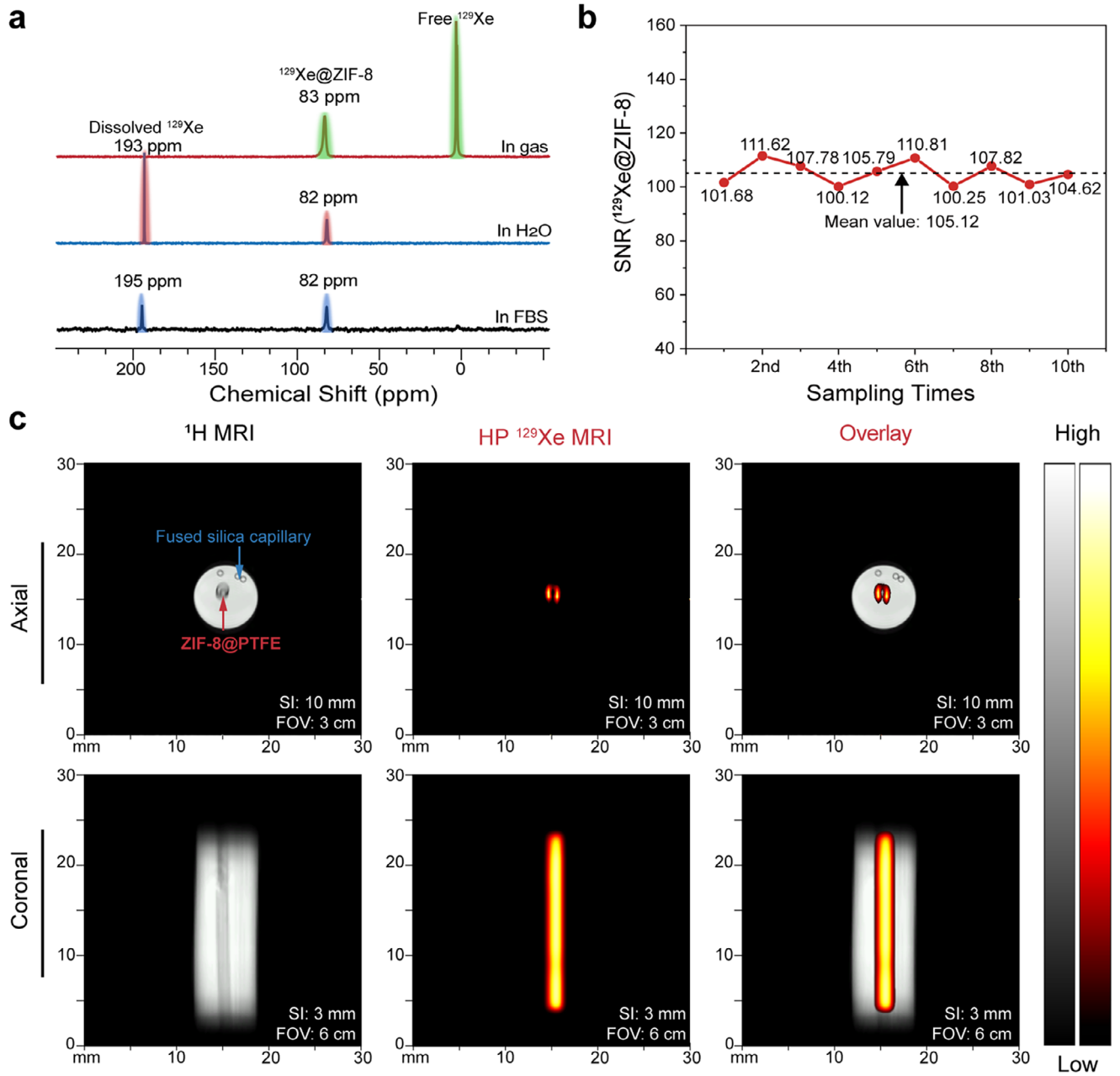

FIGURE 3 | ^{1}H/^{129}Xe MRI co-localization of ZIF-8@PTFE. (a) ^{129}Xe NMR spectra in gas, water, and FBS (NS = 1, LB = 5 Hz). (b) SNR of the ^{129}Xe@ZIF-8 signal across 10 consecutive acquisitions (NS = 1, LB = 20 Hz). (c) ^{1}H/^{129}Xe MRI of ZIF-8@PTFE in a 10 mm NMR tube containing deionized water.

The dissolved-phase ^{129}Xe peak appeared at 207.8 ppm. The lower film-bound SNR under flow may reflect reduced xenon residence time, bubble transport, or lower local dissolved-xenon availability; these contributions were not distinguished. Because direct bubbling generates nonphysiological gas-liquid interfaces, the magnitude of the SNR reduction should not be extrapolated to intravascular conditions.

We then tested co-localized imaging in the same setup. Selective excitation at the film-bound frequency yielded coating-specific ^{129}Xe images that co-registered with ^{1}H images of the lumen when the pump was running (Figure 4c). In the axial plane, the center-point offset between the ^{1}H and ^{129}Xe images was 0.26 mm. These data show that the ZIF-8 film supports ^{129}Xe-based localization in this flow simulator. They do not demonstrate physiological xenon delivery to an intravascular device.

2.4 | In Vivo Airway Localization of ZIF-8@PTFE

As an in vivo gas-contact test, we evaluated spectral selectivity and co-localization in the rat airway. Because of the narrow airway, a thin ZIF-8@PTFE segment (outer diameter 0.85 mm, inner diameter 0.5 mm) was constructed and characterized (Figure S22). The thin ZIF-8@PTFE also showed film-bound ^{129}Xe signals in gas, water, and FBS (Figure S23), with signal intensity similar to that of the 1.34 mm ZIF-8@PTFE segments under the tested conditions. Following tracheotomy, the

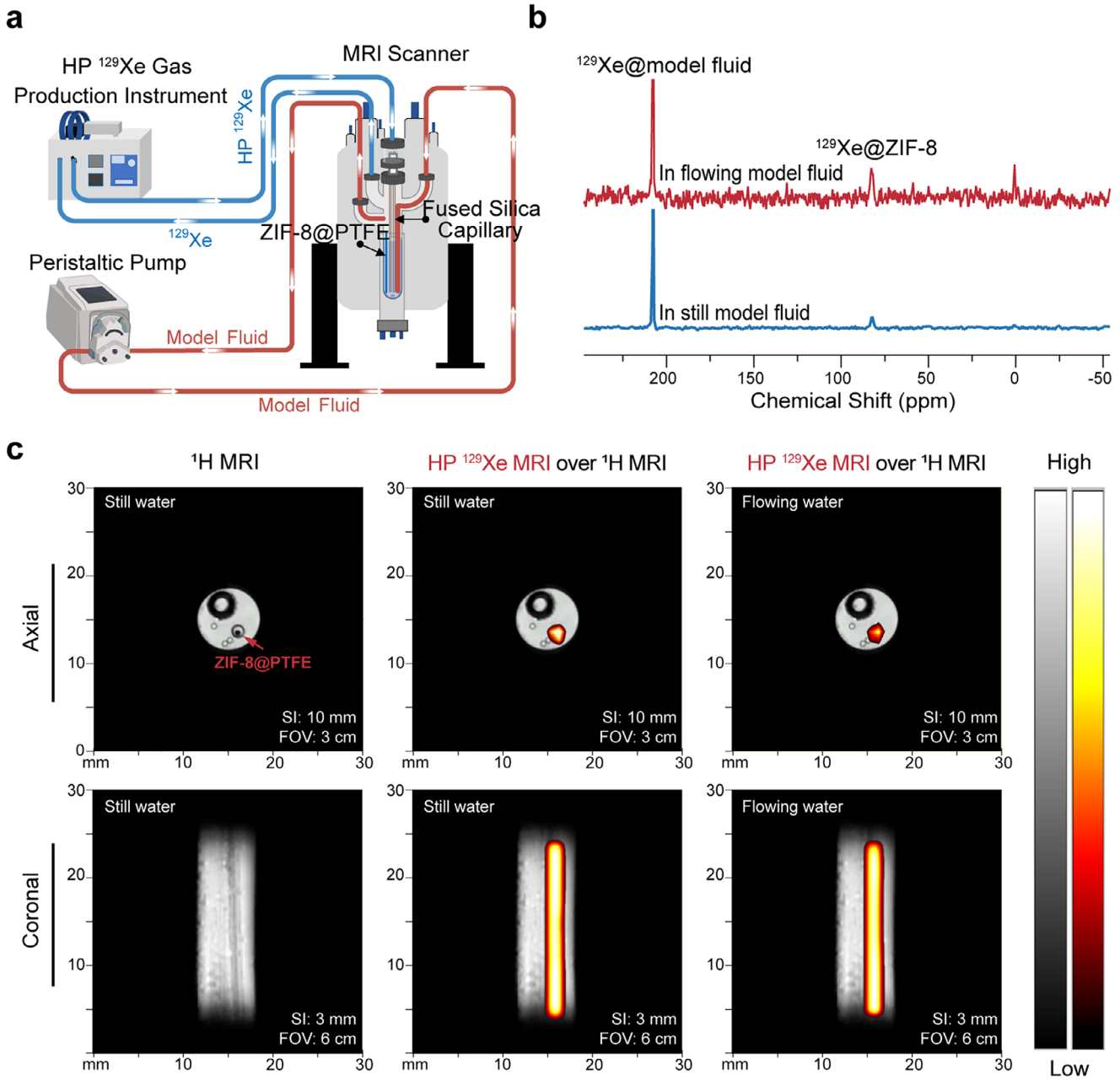

FIGURE 4 | $^{1}H/^{129}Xe$ MRI co-localization of ZIF-8@PTFE in the flow simulator. (a) Schematic of the setup. (b) HP ^{129}Xe NMR spectra in flowing (NS = 16, LB = 30 Hz) and static (NS = 8, LB = 30 Hz) model fluid; four ZIF-8@PTFE segments were used. (c) $^{1}H/^{129}Xe$ MRI of ZIF-8@PTFE during static and flowing conditions.

ZIF-8@PTFE segment was inserted to maintain an airway passage, and Sprague-Dawley rats were ventilated alternately with oxygen and ^{129}Xe. Breath-hold ^{129}Xe MRI was acquired immediately after ^{129}Xe inhalation (Figure S24). A distinct film-bound resonance from the coated segment was detected in the airway at ~92 ppm, shifted by ~10 ppm downfield relative to the value in water, consistent with a different local xenon environment (Figure S25).

Selective excitation at the film-bound frequency was used to image the coated segment on the ^{129}Xe channel, while the free-xenon signal provided airway structure (Figure 5a). The resulting coating-selective ^{129}Xe images were colorized and overlaid on ^{129}Xe lung images and on ^{1}H anatomy, yielding co-localization in the airway. The apparent width of the thin ZIF-8@PTFE segment on the ^{129}Xe image differed from its physical diameter by 61.2%. Thus, the ^{129}Xe data provide selective localization but should not be interpreted as accurate diameter measurements. Individual ^{129}Xe images in Figure 5a were acquired in 3.1 s, allowing repeated localization during placement; this acquisition does not constitute real-time device tracking.

We also assessed the ^{1}H MRI appearance by inserting a coated segment (diameter 1.34 mm) into the liver of a mouse cadaver. In this ex vivo measurement, the apparent width of ZIF-8@PTFE on the ^{1}H image differed from its physical diameter by 1.5%

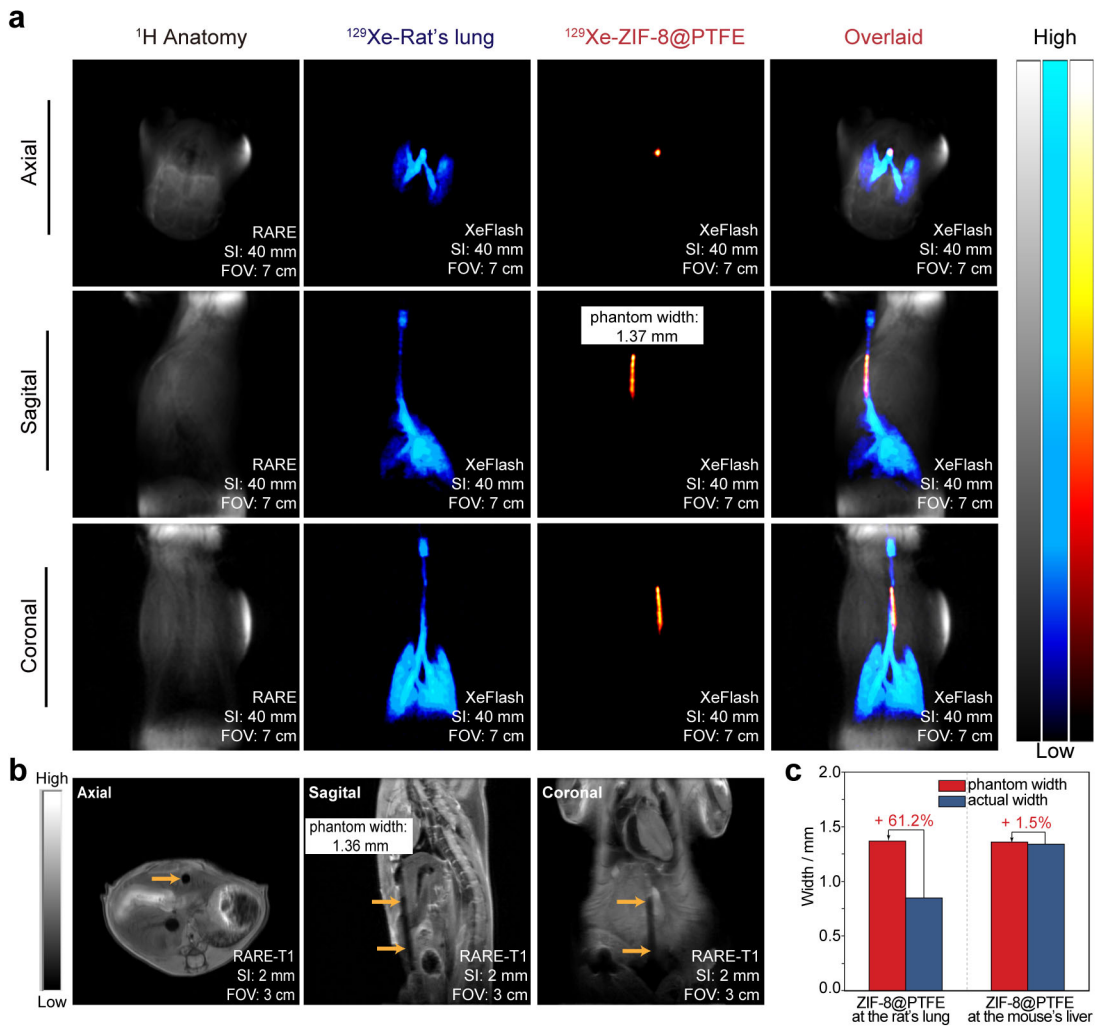

FIGURE 5 | In vivo and ex vivo $^{1}H/^{129}Xe$ MRI of ZIF-8@PTFE. (a) $^{1}H/^{129}Xe$ MRI of the rat lung and the thin ZIF-8@PTFE segment (diameter 0.85 mm) placed in the airway. (b) ^{1}H MRI of the thick ZIF-8@PTFE segment (diameter 1.34 mm) in the liver of a mouse cadaver. The yellow arrows indicate ZIF-8@PTFE. (c) Comparison of the apparent ZIF-8@PTFE width measured on MR images with the physical diameter.

(Figure 5b,c). Table 1 reports literature values descriptively; because the devices, scanners, field strengths, pulse sequences, and analysis procedures differ, these values do not constitute a matched benchmark or support quantitative ranking [17, 55–57]. No measurable temperature increase was observed for ZIF-8@PTFE under the tested 3 T sequence, whereas a nitinol guidewire surrogate equipped with a solenoid coil showed a 1.5°C temperature rise (Figure S26). This result is specific to the tested geometry and sequence and does not replace standardized RF-safety testing of a complete device.

3 | Conclusion

We report a ZIF-8 film coating on PTFE that renders a polymer surface addressable by HP ^{129}Xe MRI. The coating produced a resolved film-bound ^{129}Xe resonance in water and FBS, and selective excitation of this resonance generated positive ^{129}Xe contrast from coated PTFE segments. Conventional ^{1}H MRI supplied anatomical context and showed distinct contrast at the coated surface. In vitro imaging and flow-simulator imaging produced submillimeter center-point offsets between the ^{1}H and ^{129}Xe channels. A rat airway experiment demonstrated film-bound ^{129}Xe contrast in a living animal under direct gas contact.

The current study is a materials-and-imaging proof of concept. It uses coated PTFE segments rather than complete guidewires, and the flow simulator uses direct bubbling of HP ^{129}Xe rather than physiological xenon delivery through blood. The work does not yet demonstrate vascular navigation, physiological dissolved-xenon delivery to an intravascular device, mechanical durability under abrasion or vascular shear, quantitative particle-detachment measurements, prolonged blood compatibility, the retention of zinc in the lungs, and thrombogenicity, or standardized RF safety of a complete device. These studies are required before the approach can be evaluated as an endovascular imaging technology.

This proof-of-concept study confirms that ZIF-8 can form dense, conformal films on Zn-PDA-modified polymer surfaces, enabling ZIF-8 film coatings to render conventional polymeric device surfaces addressable via $^{1}H/^{129}Xe$ MRI. Alternative xenon-host materials may offer distinct chemical shifts, exchange kinetics, and sensitivities. Realizing such alternative coatings for devices

TABLE 1 | Descriptive comparison of apparent diameter deviations for ZIF-8@PTFE segments and literature MR-visible guidewires. The acquisition and analysis conditions differ substantially; the values are provided for orientation only and do not support matched or statistical comparison.

Designation	Category	Actual diameter (mm)		Measured diameter (mm)		Diameter deviation (%)		Imaging modality
ZIF-8@PTFE segment (This work)	Coated PTFE segment	1.34 (thick)	0.85 (thin)	1.36 (thick)	1.37 (thin)	1.5% (thick)	61.2% (thin)	$^{1}H/^{129}Xe$ MRI
MaRVis MR guidewires [55]	Passive	0.89 mm		2.00 mm		124.7%		^{1}H MRI only
Emeryglide MRWire [56]	Passive	0.89 mm		3.92 mm		340.4%		^{1}H MRI only
MaRVis MR guidewires [17]	Passive	0.89 mm		2.35 mm		164.0%		^{1}H MRI only
RF+GA35153M [57]	Active	0.89 mm		2.60 mm		192.1%		^{1}H MRI only

will demand tailored immobilization chemistries that maintain efficient xenon exchange and coating stability.

These results support MOF-film coatings as candidates for spectrally selective MRI labeling of polymer surfaces. The coated segments provide coating-specific ^{129}Xe contrast without an embedded RF conductor, while the ^{1}H channel supplies anatomy. Further development should focus on time-resolved structural and chemical stability measurements, quantitative leaching and linker-release assays, quantitative coating adhesion, particle-shedding analysis, matched imaging benchmarks, and physiological dissolved-xenon delivery experiments.

4 | Experimental Section

4.1 | Materials Used

Dopamine hydrochloride and Tris-HCl were purchased from Aladdin (Shanghai, China). $ZnCl_2$, sodium formate (HCOONa), 2-MI, anhydrous methanol (MeOH), and other chemicals used in this work were all purchased from Sinopharm Chemical Reagent Co. Ltd (Beijing, China). The PTFE heat-shrink tube (HST-PTFE (1.7:1) type) was purchased from Hongjiexin Technology Co. Ltd (Shenzhen, China).

4.2 | Modification and Activation of Zn-PDA Coating on Pristine PTFE Tube

PTFE heat-shrink tubing (used here as a cover surrogate) was cut into ~8 cm segments and sequentially sonicated in ethanol (15 min) and deionized (DI) water (15 min). Cleaned segments were immersed in 100 mL Tris–HCl buffer (10 mM, pH 8.5), to which dopamine hydrochloride (200 mg) and $ZnCl_2$ (400 mg) were added. The suspension was stirred at room temperature for 24 h. Afterward, the coated segments were rinsed repeatedly with DI water and dried at 65°C for 12 h, yielding a Zn-PDA layer. For activation, 2-MI (1.2565 g) was dissolved in 10 mL DI water. Zn-PDA-coated segments were immersed in this solution at room temperature for 5 h, then removed and washed thoroughly with DI water prior to ZIF-8 growth.

4.3 | Preparation of ZIF-8@PTFE

2-MI (5.21 g) was dissolved in 40 mL methanol. In parallel, $ZnCl_2$ (1.01 g) and HCOONa (1.45 g) were dissolved in 40 mL methanol. The two solutions were combined, mixed thoroughly, and transferred into a 100 mL Teflon-lined autoclave along with activated Zn-PDA-coated PTFE segments. The autoclave was heated to 120°C for 4 h, then cooled to room temperature. Coated segments were removed, rinsed repeatedly with DI water, and dried at 65°C overnight to yield ZIF-8@PTFE samples.

4.4 | Animal Preparation

All procedures were approved by the Review Board of the Innovation Academy for Precision Measurement Science and Technology, Chinese Academy of Sciences (approval number, APM25007A), and were conducted in accordance with the national Regulations for the Administration of Affairs Concerning Experimental Animals. Healthy female Sprague–Dawley rats (body mass = 220–240 g) and BALB/c mice (body mass = 20–22 g) were provided by the Hubei BIONT Biological Technology Co., LTD (Wuhan, Hubei, China). Before surgery, the rats were anesthetized with 5% isoflurane (RWD, Shenzhen, Guangdong, China) and maintained under 2% isoflurane anesthesia for the duration of the procedure.

Additional experiment details can be found in the Supporting Information.

4.5 | Statistical Analysis

Quantitative data are expressed as mean ± standard deviation (SD). Two-tailed Student's *t*-test was used for two-group comparisons, all performed within OriginPro2021. Significance levels are indicated by asterisks: a p-value of less than 0.05 is the benchmark for statistical significance, ** for $p < 0.01$, *** for $p < 0.001$, and **** for $p < 0.0001$. The SNR for all distinct resonance signals in hyperpolarized ^{129}Xe NMR spectra was determined using the built-in sino command within TopSpin processing software. The center-point offset between co-registered ^{129}Xe

and ^{1}H phantom images, and the measured diameter of ZIF-8@PTFE were determined using ImageJ. The actual diameter of ZIF-8@PTFE was measured with a vernier caliper.

Funding

This work is supported by the Strategic Priority Research Program, CAS (XDB0540000), National Natural Science Foundation of China (82127802, 82441015), Key Research Program of Frontier Sciences, CAS (ZDBS-LY-JSC004), Major Program (JD) of Hubei Province (2023BAA021), Hubei Provincial Natural Science Foundation of China (2026AFA096), and Scientific Instrument Developing Project of the Chinese Academy of Sciences (PTYQ2024TD0001). Q.G. and L.-S.B. acknowledge the support from the CAS Youth Interdisciplinary Team (JCTD-2022-13). Q.Z. acknowledges the support from the Youth Innovation Promotion Association, CAS (2023347).

Conflicts of Interest

The authors declare no conflict of interest.

Data Availability Statement

Research data are not shared.

References

1. M. K. Albolkany, C. Liu, Y. Wang, et al., "Molecular Surgery at Microporous MOF for Mesopore Generation and Renovation," *Angewandte Chemie International Edition* 60 (2021): 14601–14608, https://doi.org/10.1002/anie.202103104.

2. Y.-Y. Xue, X.-Y. Bai, J. Zhang, et al., "Precise Pore Space Partitions Combined With High-Density Hydrogen-Bonding Acceptors Within Metal–Organic Frameworks for Highly Efficient Acetylene Storage and Separation," *Angewandte Chemie International Edition* 60 (2021): 10122–10128, https://doi.org/10.1002/anie.202015861.

3. A. Corma, H. Garcia, and F. X. Llabres i Xamena, "Engineering Metal Organic Frameworks for Heterogeneous Catalysis," *Chemical Reviews* 110 (2010): 4606–4655, https://doi.org/10.1021/cr9003924.

4. L. E. Kreno, K. Leong, O. K. Farha, M. Allendorf, R. P. Van Duyne, and J. T. Hupp, "Metal–Organic Framework Materials as Chemical Sensors," *Chemical Reviews* 112 (2012): 1105–1125, https://doi.org/10.1021/cr200324t.

5. Y.-B. Tian, N. Vankova, P. Weidler, et al., "Oriented Growth of In-Oxo Chain Based Metal-Porphyrin Framework Thin Film for High-Sensitive Photodetector," *Advanced Science* 8 (2021): 2100548, https://doi.org/10.1002/advs.202100548.

6. Y. Zhu, N. Xin, Z. Qiao, et al., "Bioactive MOFs Based Theranostic Agent for Highly Effective Combination of Multimodal Imaging and Chemo-Phototherapy," *Advanced Healthcare Materials* 9 (2020): 2000205, https://doi.org/10.1002/adhm.202000205.

7. C. Wang, X. Jia, W. Zhen, M. Zhang, and X. Jiang, "Small-Sized MOF-Constructed Multifunctional Diagnosis and Therapy Platform for Tumor," *ACS Biomaterials Science & Engineering* 5 (2019): 4435–4441, https://doi.org/10.1021/acsbiomaterials.9b00813.

8. X. Deng, T. Liu, and Y. Zhu, "Ca & Mn Dual-Ion Hybrid Nanostimulator Boosting Anti-Tumor Immunity via Ferroptosis and Innate Immunity Awakening," *Bioactive Materials* 33 (2024): 483–496, https://doi.org/10.1016/j.bioactmat.2023.11.017.

9. G. H. Griffin, K. J. T. Anderson, and G. A. Wright, "Miniaturizing Floating Traps to Increase RF Safety of Magnetic-Resonance-Guided Percutaneous Procedures," *IEEE Transactions on Biomedical Engineering* 64 (2017): 329–340, https://doi.org/10.1109/TBME.2016.2553680.

10. J. G. Miller, M. Li, D. Mazilu, T. Hunt, and K. A. Horvath, "Real-Time Magnetic Resonance Imaging–Guided Transcatheter Aortic Valve Replacement," *The Journal of Thoracic and Cardiovascular Surgery* 151 (2016): 1269–1277, https://doi.org/10.1016/j.jtcvs.2015.11.024.

11. M. Etezadi-Amoli, P. Stang, A. Kerr, J. Pauly, and G. Scott, "Interventional Device Visualization With Toroidal Transceiver and Optically Coupled Current Sensor for Radiofrequency Safety Monitoring," *Magnetic Resonance in Medicine* 73 (2015): 1315–1327, https://doi.org/10.1002/mrm.25187.

12. Y. Meng, F. Zhang, H. Gu, et al., "Intravascular 3.0 T MRI Using an Imaging-Guidewire: A Feasibility Study in Swine," *Applied Magnetic Resonance* 40 (2011): 105–112, https://doi.org/10.1007/s00723-010-0186-0.

13. G. C. McKinnon, J. F. Debatin, D. A. Leung, S. Wildermuth, D. J. Holtz, and G. K. vonSchulthess, "Towards Active Guidewire Visualization in Interventional Magnetic Resonance Imaging," *Magnetic Resonance Materials in Physics, Biology and Medicine* 4 (1996): 13–18, https://doi.org/10.1007/BF01759775.

14. A. Alipour, E. S. Meyer, C. L. Dumoulin, et al., "MRI Conditional Actively Tracked Metallic Electrophysiology Catheters and Guidewires With Miniature Tethered Radio-Frequency Traps: Theory, Design, and Validation," *IEEE Transactions on Biomedical Engineering* 67 (2020): 1616–1627, https://doi.org/10.1109/TBME.2019.2941460.

15. D. K. Yildirim, D. Uzun, C. G. Bruce, et al., "An Interventional MRI Guidewire Combining Profile and Tip Conspicuity for Catheterization at 0.55T," *Magnetic Resonance in Medicine* 89 (2023): 845–858, https://doi.org/10.1002/mrm.29466.

16. F. Wegner, K. Lüdtke-Buzug, S. Cremers, et al., "Bimodal Interventional Instrument Markers for Magnetic Particle Imaging and Magnetic Resonance Imaging—A Proof-of-Concept Study," *Nanomaterials* 12 (2022): 1758, https://doi.org/10.3390/nano12101758.

17. X. Li, L. E. Perotti, J. A. Martinez, S. M. Duarte-Vogel, D. B. Ennis, and H. H. Wu, "Real-Time 3T MRI-Guided Cardiovascular Catheterization in a Porcine Model Using a Glass-Fiber Epoxy-Based Guidewire," *PLoS ONE* 15 (2020): 0229711, https://doi.org/10.1371/journal.pone.0229711.

18. K. E. Schleicher, M. Bock, K. During, S. Kroboth, and A. J. Krafft, "Radial MRI With Variable Echo Times: Reducing the Orientation Dependency of Susceptibility Artifacts of an MR-Safe Guidewire," *Magnetic Resonance Materials in Physics, Biology and Medicine* 31 (2018): 235–242, https://doi.org/10.1007/s10334-017-0645-9.

19. E. Blanco, V. Segura-Ibarra, D. Bawa, et al., "Functionalization of Endovascular Devices With Superparamagnetic Iron Oxide Nanoparticles for Interventional Cardiovascular Magnetic Resonance Imaging," *Biomedical Microdevices* 21 (2019): 38, https://doi.org/10.1007/s10544-019-0393-x.

20. J. Haegele, N. Panagiotopoulos, S. Cremers, et al., "Magnetic Particle Imaging: A Resovist Based Marking Technology for Guide Wires and Catheters for Vascular Interventions," *IEEE Transactions on Medical Imaging* 35 (2016): 2312–2318, https://doi.org/10.1109/TMI.2016.2559538.

21. F. Godart, J. P. Beregi, L. Nicol, et al., "MR-Guided Balloon Angioplasty of Stenosed Aorta: In Vivo Evaluation Using Near-Standard Instruments and a Passive Tracking Technique," *Journal of Magnetic Resonance Imaging* 12 (2000): 639–644, https://doi.org/10.1002/1522-2586(200010)12:4⟨639.

22. M. A. Rube, B. F. Cox, M. Gueorguieva, D. Kakchingtabam, P. Andre, and A. Melzer, "Iron-Platinum Alloy Nanoparticles for Guidewire and Resonant Markers for Catheter Localization During Interventional MRI," *Biomedical Engineering / Biomedizinische Technik* 57 (2012): 976–976, https://doi.org/10.1515/bmt-2012-4397.

23. C. J. Bakker, H. F. Smits, C. Bos, et al., "MR-Guided Balloon Angioplasty: In Vitro Demonstration of the Potential of MRI for Guiding, Monitoring, and Evaluating Endovascular Interventions," *Journal of Magnetic Resonance Imaging* 8 (1998): 245–250, https://doi.org/10.1002/jmri.1880080141.

24. S. Xiao, H. Deng, C. Duan, et al., "Highly and Adaptively Undersampling Pattern for Pulmonary Hyperpolarized ^{129}Xe Dynamic MRI," *IEEE Transactions on Medical Imaging* 38 (2019): 1240–1250, https://doi.org/10.1109/TMI.2018.2882209.

25. T. G. Walker and W. Happer, "Spin-Exchange Optical Pumping of Noble-Gas Nuclei," *Reviews of Modern Physics* 69 (1997): 629–642, https://doi.org/10.1103/RevModPhys.69.629.

26. M. He, B. Driehuys, L. Que, and Y.-C. T. Huang, "Using Hyperpolarized ^{129}Xe MRI to Quantify the Pulmonary Ventilation Distribution," *Academic Radiology* 23 (2016): 1521–1531, https://doi.org/10.1016/j.acra.2016.07.014.

27. S. Svenningsen, M. McIntosh, A. Ouriadov, et al., "Reproducibility of Hyperpolarized ^{129}Xe MRI Ventilation Defect Percent in Severe Asthma to Evaluate Clinical Trial Feasibility," *Academic Radiology* 28 (2021): 817–826, https://doi.org/10.1016/j.acra.2020.04.025.

28. H. Li, H. Li, L. Fan, et al., "Dynamic Ventilation Functional MRI of the Lung With Sub-Millimeter Spatial Resolution and Millisecond Temporal Resolution," *Science Bulletin* 70 (2025): 4142–4145, https://doi.org/10.1016/j.scib.2025.05.014.

29. M. Zhang, H. Li, Y. Xiao, et al., "Assessment of Global and Regional Lung Compliance in Pulmonary Fibrosis With Hyperpolarized Gas MRI," *Journal of Magnetic Resonance Imaging* 61 (2025): 1404–1415, https://doi.org/10.1002/jmri.29497.

30. Y. Fang, H. Li, L. Shen, et al., "Rapid Pulmonary 129 Xe Ventilation MRI of Discharged COVID-19 Patients With Zigzag Sampling," *Magnetic Resonance in Medicine* 92 (2024): 956–966, https://doi.org/10.1002/mrm.30120.

31. L. Shen, H. Li, Y. Fang, et al., "Hyperpolarized 129 Xe Diffusion-Weighted MRI of the Lung With 3D Golden-Angle Radial Sampling and Keyhole Reconstruction," *Medical Physics* 52 (2025): 4068–4078, https://doi.org/10.1002/mp.17719.

32. Q. Rao, H. Li, Q. Zhou, et al., "Assessment of Pulmonary Physiological Changes Caused by Aging, Cigarette Smoking, and COPD With Hyperpolarized ^{129}Xe Magnetic Resonance," *European Radiology* 34 (2024): 7450–7459, https://doi.org/10.1007/s00330-024-10800-w.

33. H. Li, H. Li, M. Zhang, C. Huang, and X. Zhou, "Direct Imaging of Pulmonary Gas Exchange With Hyperpolarized Xenon MRI," *The Innovation* 5 (2024): 100720, https://doi.org/10.1016/j.xinn.2024.100720.

34. M. Zhang, H. Li, H. Li, et al., "Dynamic Evaluation of Acute Lung Injury Using Hyperpolarized ^{129}Xe Magnetic Resonance," *NMR in Biomedicine* 37 (2024): 5078, https://doi.org/10.1002/nbm.5078.

35. B. Zanette, E. Stirrat, S. Jelveh, A. Hope, and G. Santyr, "Physiological Gas Exchange Mapping of Hyperpolarized 129 Xe Using Spiral- IDEAL and MOXE in a Model of Regional Radiation-Induced Lung Injury," *Medical Physics* 45 (2018): 803–816, https://doi.org/10.1002/mp.12730.

36. B. Zanette and G. Santyr, "Accelerated Interleaved Spiral-IDEAL Imaging of Hyperpolarized 129 Xe for Parametric gas Exchange Mapping in Humans," *Magnetic Resonance in Medicine* 82 (2019): 1113–1119, https://doi.org/10.1002/mrm.27765.

37. Q. Zeng, Z. Wang, Q. Guo, et al., "Water-Stable Metal-Organic Framework for Hyperpolarized Xenon MRI in Aqueous Solution," *Chemical Research in Chinese Universities* 41 (2025): 305–312, https://doi.org/10.1007/s40242-025-4234-6.

38. Q. Zeng, B. Bie, Q. Guo, et al., "Hyperpolarized Xe NMR Signal Advancement by Metal-Organic Framework Entrapment in Aqueous Solution," *Proceedings of the National Academy of Sciences* 117 (2020): 17558–17563, https://doi.org/10.1073/pnas.2004121117.

39. Q. Zeng, Q. Yue, M. Zhang, et al., "Multivariate Metal-Organic Frameworks Enable Chemical Shift-Encoded MRI With Femtomolar Sensitivity for Biological Systems," *Nature Communications* 16 (2025): 6832, https://doi.org/10.1038/s41467-025-62110-4.

40. S. R. Veeram Reddy, Y. Arar, R. A. Zahr, et al., "Invasive Cardiovascular Magnetic Resonance (iCMR) for Diagnostic Right and Left Heart Catheterization Using an MR-Conditional Guidewire and Passive Visualization in Congenital Heart Disease," *Journal of Cardiovascular Magnetic Resonance* 22 (2020): 20, https://doi.org/10.1186/s12968-020-0605-9.

41. X. Ruan, X. Zhang, Z. Zhou, et al., "ZIF-8 Heterogeneous Nucleation and Growth Mechanism on Zn(II)-Doped Polydopamine for Composite Membrane Fabrication," *Separation and Purification Technology* 214 (2019): 95–103, https://doi.org/10.1016/j.seppur.2018.02.049.

42. M. C. McCarthy, V. Varela-Guerrero, G. V. Barnett, and H.-K. Jeong, "Synthesis of Zeolitic Imidazolate Framework Films and Membranes With Controlled Microstructures," *Langmuir* 26 (2010): 14636–14641, https://doi.org/10.1021/la102409e.

43. M. M. Spence, S. M. Rubin, I. E. Dimitrov, et al., "Functionalized Xenon as a Biosensor," *Proceedings of the National Academy of Sciences* 98 (2001): 10654–10657, https://doi.org/10.1073/pnas.191368398.

44. T. K. Stevens, R. M. Ramirez, and A. Pines, "Nanoemulsion Contrast Agents With Sub-Picomolar Sensitivity for Xenon NMR," *Journal of the American Chemical Society* 135 (2013): 9576–9579, https://doi.org/10.1021/ja402885q.

45. M. G. Shapiro, R. M. Ramirez, L. J. Sperling, et al., "Genetically Encoded Reporters for Hyperpolarized Xenon Magnetic Resonance Imaging," *Nature Chemistry* 6 (2014): 629–634, https://doi.org/10.1038/NCHEM.1934.

46. M. Kunth, C. Witte, A. Hennig, and L. Schröder, "Identification, Classification, and Signal Amplification Capabilities of High-Turnover Gas Binding Hosts in Ultra-Sensitive NMR," *Chemical Science* 6 (2015): 6069–6075, https://doi.org/10.1039/c5sc01400j.

47. J. Roukala, J. F. Zhu, C. Giri, K. Rissanen, P. Lantto, and V. V. Telkki, "Encapsulation of Xenon by a Self-Assembled Fe_4L_6 Metallosupramolecular Cage," *Journal of the American Chemical Society* 137 (2015): 2464–2467, https://doi.org/10.1021/ja5130176.

48. Y. Wang, B. W. Roose, E. J. Palovcak, V. Carnevale, and I. J. Dmochowski, "A Genetically Encoded β-Lactamase Reporter for Ultrasensitive 129 Xe NMR in Mammalian Cells," *Angewandte Chemie International Edition* 55 (2016): 8984–8987, https://doi.org/10.1002/anie.201604055.

49. M. J. Sever, J. T. Weisser, J. Monahan, S. Srinivasan, and J. J. Wilker, "Metal-Mediated Cross-Linking in the Generation of a Marine-Mussel Adhesive," *Angewandte Chemie International Edition* 43 (2004): 448–450, https://doi.org/10.1002/anie.200352759.

50. H. Wu, J. Ang, J. Kong, C. Zhao, Y. Du, and X. Lu, "One-pot synthesis of polydopamine–Zn complex antifouling coatings on membranes for ultrafiltration Under harsh conditions," *RSC Advances* 6 (2016): 103390–103398, https://doi.org/10.1039/c6ra19858a.

51. X. Huang, Y. Lin, J. Zhang, and X. Chen, "Ligand-Directed Strategy for Zeolite-Type Metal–Organic Frameworks: Zinc(II) Imidazolates With Unusual Zeolitic Topologies," *Angewandte Chemie International Edition* 45 (2006): 1557–1559, https://doi.org/10.1002/anie.200503778.

52. K. S. Park, Z. Ni, A. P. Côté, et al., "Exceptional Chemical and Thermal Stability of Zeolitic Imidazolate Frameworks," *Proceedings of the National Academy of Sciences* 103 (2006): 10186–10191, https://doi.org/10.1073/pnas.0602439103.

53. P. Chen, M. He, B. Chen, and B. Hu, "Size- and Dose-Dependent Cytotoxicity of ZIF-8 Based on Single Cell Analysis," *Ecotoxicology and Environmental Safety* 205 (2020): 111110, https://doi.org/10.1016/j.ecoenv.2020.111110.

54. M. Hoop, C. F. Walde, R. Riccò, et al., "Biocompatibility Characteristics of the Metal Organic Framework ZIF-8 for Therapeutical Applications," *Applied Materials Today* 11 (2018): 13–21, https://doi.org/10.1016/j.apmt.2017.12.014.

55. A. Massmann, A. Buecker, and G. K. Schneider, "Glass-Fiber–Based MR-Safe Guidewire for MR Imaging–guided Endovascular Interventions: In Vitro and Preclinical in Vivo Feasibility Study," *Radiology* 284 (2017): 541–551, https://doi.org/10.1148/radiol.2017152742.

56. A. K. Armstrong, Y. Liu, J. M. Kelly, et al., "Feasibility of Magnetic Resonance Imaging-Guided Cardiac Catheterization, Angioplasty, and Stenting in a Commercial

Wide-Bore 0.55 T Scanner," *Journal of Cardiovascular Magnetic Resonance* 27 (2025): 101858, https://doi.org/10.1016/j.jocmr.2025.101858.

57. F. Godinez, G. Scott, F. Padormo, J. V. Hajnal, and S. J. Malik, "Safe Guidewire Visualization Using the Modes of a PTx Transmit Array MR System," *Magnetic Resonance in Medicine* 83 (2020): 2343–2355, https://doi.org/10.1002/mrm.28069.

Supporting Information

Additional supporting information can be found online in the Supporting Information section.

Supporting File: smll75746-sup-0001-SuppMat.docx.